JOURNAL OF MATERIALS SCIENCE **35** (2000) 5359–5369

Multi-length scale modeling of CVD of diamond

Part I *A combined reactor-scale/atomic-scale analysis*

M. GRUJICIC, S. G. LAI
Program in Materials Science and Engineering, Department of Mechanical Engineering, 241 Fluor Daniel Building, Clemson University, Clemson, S.C. 29634-0921
E-mail: mica@ces.clemson.edu

Chemical vapor deposition of the (111)- and (100)-oriented single-crystalline diamond films is studied by combining a reactor-scale model with an atomic-scale model. The reactor-scale model is based on the solution of a continuum fluid-flow/heat-transfer boundary value problem for a reactive gas in contact with a deposition surface. The atomic-scale modeling is carried out using a kinetic Monte Carlo method. A consistency between the two modeling schemes is achieved by: (a) using the reactor-scale modeling predictions as input to the atomic-scale modeling scheme and; (b) using the atomic-scale modeling results to identify the surface reactions which govern and, hence, should be used in reactor-scale modeling of the deposition of (111)- and (100)-oriented diamond films. It is found that by properly combining the two types of models, consistent predictions for the film deposition rates can be obtained over a relatively large range of the CVD processing conditions. In addition, different phenomena are found to govern the deposition process for (111)- and (100)-oriented films. In the case of (111)-oriented films, the film growth rate appears to be controlled by the nucleation of new layers. Contrary in the case of (100)-oriented films, both the nucleation and growth processes seem to have comparable effects.

1. Introduction

Processing of diamond films by chemical vapor deposition (CVD) from a precursor gas mixture containing a small amount of hydrocarbon (usually methane, acetylene, etc.) and hydrogen as the carrier gas at subambient pressures of 1–200 Torr has become commercially viable over the last decade [e.g. 1–3]. The gas mixture is typically heated using hot filaments, plasmas, combustion flames, and other means to promote dissociation of some of the molecular hydrogen into atomic hydrogen and formation of various hydrocarbon radicals. Despite the fact that under the standard CVD processing conditions graphite is the stable form of carbon, atomic hydrogen bonds with carbon atoms on the surface and passivates it by converting the graphite-type sp^2-bonded surface carbon atoms into the sp^3-bonded diamond-type carbon atoms [2, 3]. While it is well-established that chemical vapor deposition of diamond occurs by the incorporation of chemisorbed hydrocarbon radicals, the mechanism of the diamond growth is still not well understood. This is primarily caused by the fact that the atomic-scale events which lead to diamond growth are difficult to study *in situ*. Hence, the current understanding of diamond growth has been primarily gained through the use of computer modeling and simulations and/or from the interpretation of *ex situ* experimental data.

Several different modeling approaches have been used to analyze the diamond growth process. Some of the models [e.g. 4, 5] deal with fluid dynamics and thermal energy effects of the reactive gas flow at the CVD-reactor length scale and allow only average film growth rates to be determined. In other words, these models fail to account for the effects of surface morphology on the deposition rate and the extent of defect generation during the film growth. At the other length-scale extreme, there is a variety of the models which deal with the CVD process at the atomic scale. Among these models, some deal with the surface energetics and are primarily used to determine kinetic parameters of the individual surface reactions [6–9] and to examine the stability of various surface configurations [10–16]. Also molecular dynamics simulations are used to model the deposition of diamond single-crystalline films but only over a few milliseconds of growth time [e.g.17]. This limitation is overcome by Battaile *et al*. [18] and Grujicic and Lai [19], who applied a kinetic Monte Carlo method to carry out three-dimensional atomic-scale simulations of (100)- and (111)-oriented diamond single-crystalline films.

In the present two-part paper a multi-length scale approach is used to study the CVD of polycrystalline diamond films. First, the CVD process is analyzed at the reactor-scale by solving the appropriate boundary value problem for a reactive gas mixture in contact with a deposition surface. In order to account for the differences between growth rates of the (111)- and (100)-oriented facets of the film surface, the boundary

conditions at the deposition surface are adjusted in the two cases to take into account the details of the surface reactions and surface morphology. Next, atomic-scale modeling of the growth of (111)- and (100)-oriented diamond films is carried out. Coupling between the reactor-scale and the atomic-scale models, which is the subject of Part I of this two-part paper, is accomplished by: (a) using the species concentration at the deposition surface obtained via the reactor-scale modeling as the boundary conditions for the atomic-scale modeling and; (b) by enforcing that the (111)- and (100)-surface growth rates predicted by the two modeling schemes are respectively compatible. In Part II of this two-part paper [20], coupling between the atomic-scale and grain-scale models is carried out in order to analyze the evolution of grain structure and film texture during CVD of the polycrystalline diamond films.

The organization of the paper is as following: In Section 2, a reactor-scale model is developed and applied to analyze the deposition of diamond films in a rotating-disk CVD reactor. Atomic-scale modeling of the CVD process via a kinetic Monte Carlo method is introduced and applied to the (100)- and (111)-oriented diamond films in Section 3. A consistency between the reactor-scale and the atomic-scale models predictions is also discussed in Section 3. The main conclusions resulted from the present work are summarized in Section 4.

2. Reactor-scale modeling of CVD

2.1. General consideration

The reactor-scale modeling of the diamond CVD process is carried out for a standard rotating-disk hot-filament CVD reactor. The rotating-disk hot-filament CVD reactor is one in which a heated disk-shape substrate spins in an cylindrical enclosure through which the reacting gas flows, Fig. 1. It is well established [e.g. 21] that the species and temperature gradients normal to the disk are equal everywhere on the disk. This gives rise to a very attractive uniform distribution of the deposition rates on the substrate and simplifies the modeling considerably.

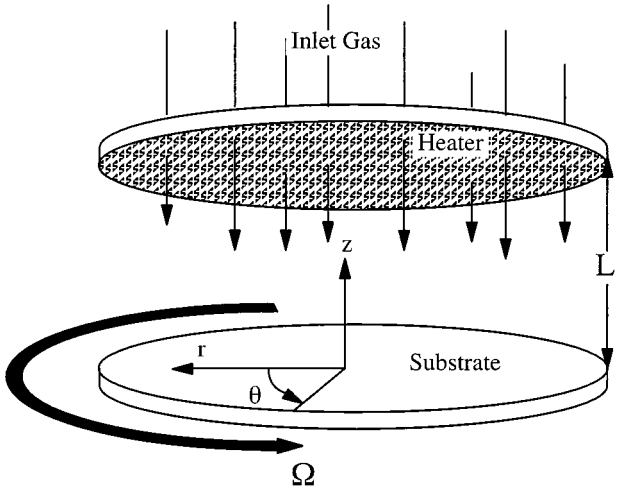

Figure 1 A schematic of the rotating-disk hot-filament CVD reactor and the associated coordinate system.

An infinite-radius disk rotating below a fluid medium is a classic problem in fluid mechanics [22–29]. For this problem the Navier-Stokes equations can be solved to obtain the exact solution. This allows the heat and mass transfer near an infinite-radius rotating disk to be studied extensively [25, 26]. As far as the application of the rotating-disk solution to CVD, Olander [27, 28] used it to analyze the germanium-iodine system, while Pollard and Newman [29] and Hitchman [30] utilized it to study the deposition of Si from $SiCl_4$. In these studies the von Karman similarity method for isothermal flow [31] is extended to include the energy and species conservation equations and to account for temperature dependence of the fluid properties, resulting in an ordinary differential equation boundary-value problem for the mass, momentum, heat and species transfer.

In the present work, the method initially proposed by Evans and Greif [31] and subsequently extended by Coltrin *et al*. [4] to include the coupling between fluid flow and chemical kinetics is used to analyze the CVD process. The method accounts for production/depletion of the species due to chemical reactions in the gas phase and at the substrate/film surface and for the convective and diffusive transport of species within the gas phase and to the deposition surface. A brief overview of the method and of its numerical implementation is given in Appendix. The model allows determination of surface coverages, deposition rates, gas-phase species concentration profiles, gas velocity profiles, and temperature profiles as a function of the process parameters such as the temperature and the rotation speed of the disk, reactor pressure, and inlet gas flow rates and species mass fractions.

34 gas-phase reactions as summarized in Table I of Coltrin and Dandy [32] are used in the present case. Arrhenius coefficients A_i, β_i and E_i which define the temperature dependence of the reaction rate constants, Equ. (15), polynomial coefficients accounting for the temperature dependence of specific heat, standard-state enthalpies and entropies of all the gas-phase species are taken from CHEMKIN II database [33].

Complex phenomena occurring at the deposition surface involving gas-phase, surface and bulk species are described using surface chemical reactions, Table I. Symbols, G, S and D in the parenthesis refer respectively to the gas-phase, surface and diamond (bulk) species, while R, R2 and R3 stand for single, double and triple radicals, respectively. All the parameters required to quantify the rates of the surface reactions are obtained by combining the information from SURFACE CHEMKIN II with the ones reported by Battaile *et al*. [18].

It is well-established [34] that the surface of polycrystalline diamond films is generally faceted with (111) and (100) planes. It is also well documented that the growth rates of (111)- and (100)-oriented single-crystalline diamond films can be quite different under the nominally identical processing condition [35]. The model derived in the previous section does not take into account neither the single-crystalline vs. polycrystalline nature of the film, nor its crystallographic orientation. To overcome this limitation, a detailed atomic-scale analysis of the surface reactions listed in Table I

TABLE I Surface reactions associated with CVD of diamond. The symbols in the parenthesis are as following: S-surface species, R-radical, G-gas, D-diamond

Reaction Number	Reaction Formula	Substrate Orientation
1	$CH(S) + H(G) \leftrightarrow C(S,R) + H_2(G)$	(111),(100)
2	$CH(S,R) + H(G) \leftrightarrow C(S,R2) + H_2(G)$	(111),(100)
3	$CH_2(S) + H(G) \leftrightarrow CH(S,R) + H_2(G)$	(111),(100)
4	$CHC_xH_y(S) + H(G) \leftrightarrow CC_xH_y(S,R) + H_2(G)$	(111),(100)
5	$C(S,R) + H(G) \leftrightarrow CH(S)$	(111),(100)
6	$C(S,R2) + H(G) \leftrightarrow CH(S,R)$	(111),(100)
7	$CH(S,R) + H(G) \leftrightarrow CH_2(S)$	(111),(100)
8	$CC_xH_y(S) + H(G) \leftrightarrow CHC_xH_y(S)$	(111),(100)
9	$CCH_2(S) + H(G) \leftrightarrow C(S,R) + CH_3(G)$	(111),(100)
10	$CCH_2(S,R) + H(G) \leftrightarrow C(S,R2) + CH_3(G)$	(111),(100)
11	$CHCH_2(S) + H(G) \leftrightarrow CH(S,R) + CH_3(G)$	(111),(100)
12	$CCH_2C_xH_y(S) + H(G) \leftrightarrow CC_xH_y(S,R) + CH_3(G)$	(111),(100)
13	$C(S,R) + CH_3(G) \leftrightarrow CCH_3(S)$	(111),(100)
14	$C(S,R2) + CH_3(G) \leftrightarrow CCH_3(S,R)$	(111),(100)
15	$CH(S,R) + C_3(G) \leftrightarrow CHCH_3(S)$	(111),(100)
16	$CC_xH_y(S) + CH_3(G) \leftrightarrow CC_xH_yCH_3(S)$	(111),(100)
17	$C(S,R) + C_2H_2(G) \leftrightarrow CC_2H_2(S)$	(111)
18	$C(S,R2) + C_2H_2(G) \leftrightarrow CC_2H_2(S,R)$	(111)
19	$CH(S,R) + C_2H_2(G) \leftrightarrow CHC_2H_2(S)$	(111)
20	$CC_xH_y(S) + C_2H_2(G) \leftrightarrow CC_xH_yC_2H_2(S)$	(111)
21	$CCH_y(S) + H(G) \leftrightarrow CCH_{y-1}(S) + H_2(G)$	(111),(100)
22	$CCH_y(S,R) + H(G) \leftrightarrow CCH_{y-1}(S,R) + H_2(G)$	(111),(100)
23	$CHCH_y(S) + H(G) \leftrightarrow CHCH_{y-1}(S) + H_2(G)$	(111),(100)
24	$CCH_zC_xH_y(S) + H(G) \leftrightarrow CCH_{z-1}C_xH_y(S) + H_2(G)$	(111),(100)
25	$CCH_y(S) + H(G) \leftrightarrow CCH_{y+1}(S)$	(111),(100)
26	$CCH_y(S,R) + H(G) \leftrightarrow CCH_{y+1}(S,R)$	(111),(100)
27	$CHCH_y(S) + H(G) \leftrightarrow CHCH_{y+1}(S)$	(111),(100)
28	$CCH_zC_xH_y(S) + H(G) \leftrightarrow CCH_{z+1}C_xH_y(S)$	(111),(100)
29	$CC_2H_y(S) + H(G) \leftrightarrow CC_2H_{y-1}(S) + H_2(G)$	(111)
30	$CC_2H_y(S,R) + H(G) \leftrightarrow CC_2H_{y-1}(S,R) + H_2(G)$	(111)
31	$CHC_2H_y(S) + H(G) \leftrightarrow CHC_2H_{y-1}(S) + H_2(G)$	(111)
32	$CC_2H_zC_xH_y(S) + H(G) \leftrightarrow CC_2H_{z-1}C_xH_y(S) + H_2(G)$	(111)
33	$CC_2H_y(S) + H(G) \leftrightarrow CC_2H_{y+1}(S)$	(111)
34	$CC_2H_y(S,R) + H(G) \leftrightarrow CC_2H_{y+1}(S,R)$	(111)
35	$CHC_2H_y(S) + H(G) \leftrightarrow CHC_2H_{y+1}(S)$	(111)
36	$CC_2H_zC_xH_y(S) + H(G) \leftrightarrow CC_2H_{z+1}C_xH_y(S)$	(111)
37	$CCH_y(S) + CH_3(G) \leftrightarrow CC_2H_{y+3}(S)$	(100)
38	$CCH_y(S,R) + CH_3(G) \leftrightarrow CC_2H_{y+3}(S,R)$	(100)
39	$CHCH_y(S) + CH_3(G) \leftrightarrow CHC_2H_{y+3}(S)$	(100)
40	$CCH_zC_xH_y(S,R) + CH_3(G) \leftrightarrow CC_2H_{z+3}C_xH_y(S,R)$	(100)
41	$C\text{-}C(S,R2) \leftrightarrow 2C(S,R2)$	(100)
42	$C\text{-}CH(S,R) \leftrightarrow CH(S,R) + C(S,R2)$	(100)
43	$CH\text{-}CH(S) \rightarrow 2CH(S,R)$	(100)
44	$C(S,R) + CCH_2(S,R) \rightarrow C(D) + CH_2(S) + C(D)$	(100)
45	$C(S,R) + CCH_2C_xH_y(S) \rightarrow C(D) + CH_2(S) + CC_xH_y(S)$	(100)
46	$C(S,R) + CCH_2H(S,R) \rightarrow C(D) + CH_2(S) + CH(S)$	(100)
47	$C(S,R) + CCH_2(S,R) \rightarrow C(D) + CH_2(S) + C(S,R)$	(100)
48	$CC_xH_y(S) + CCH_2(S,R) \rightarrow CC_xH_y(S) + CH_2(S) + C(D)$	(100)
49	$CH(S,R) + CCH_2(S,R) \rightarrow CH(S) + CH_2(S) + C(D)$	(100)
50	$C(S,R2) + CCH_2(S,R) \rightarrow C(S,R) + CH_2(S) + C(D)$	(100)
51	$CC_xH_y(S,R) + CCH_2C_xH_y(S) \rightarrow CC_xH_y(S) + CH_2(S) + CC_xH_y(S)$	(100)
52	$CC_xH_y(S,R) + CCH_2H(S,R) \rightarrow CC_xH_y(S) + CH_2(S) + CH(S)$	(100)
53	$CC_xH_y(S,R) + CCH_2(S,R) \rightarrow CC_xH_y(S) + CH_2(S) + C(S,R)$	(100)
54	$CH(S,R) + CCH_2C_xH_y(S) \rightarrow CH(S) + CH_2(S) + CC_xH_y(S)$	(100)
55	$CH(S,R) + CCH_2H(S,R) \rightarrow CH(S) + CH_2(S) + CH(S)$	(100)
56	$CH(S,R) + CCH_2(S,R) \rightarrow CH(S) + CH_2(S) + C(S,R)$	(100)
57	$C(S,R2) + CCH_2C_xH_y(S) \rightarrow C(S,R) + CH_2(S) + CC_xH_y(S)$	(100)
58	$C(S,R2) + CCH_2H(S,R) \rightarrow C(S,R) + CH_2(S) + CH(S)$	(100)
59	$C(S,R2) + CCH_2(S,R) \rightarrow C(S,R) + CH_2(S) + C(S,R)$	(100)
60	$CH(S,R) + CHC_2H_2(S,R) \rightarrow CH(S) + CH_2(S,R) + CH(S)$	(100)
61	$CCH_2(S) + CC_2H_3(S) \rightarrow C(D) + C(D) + CH_2(S) + CH(S,R) + CH_2(S) + C(D)$	(111)
62	$C{-}CH(S) + H(G) \leftrightarrow C{-}C(S,R) + H_2(G)$	(100)
63	$C{-}C(S,R) + H(G) \leftrightarrow C{-}CH(S)$	(100)
64	$C{-}CCH_2(S) + H(G) \leftrightarrow C{-}C(S,R) + CH_3(G)$	(100)
65	$C{-}C(S,R) + CH_3(G) \leftrightarrow C{-}CCH_3(S)$	(100)
66	$C{-}CCH_y(S) + H(G) \leftrightarrow C{-}CCH_y + H_2(G)$	(100)
67	$C{-}CCH_y(S) + H(G) \leftrightarrow C{-}CCH_{y+1}(S)$	(100)
68	$C{-}CCH_2(S) + C{-}C(S,R) \rightarrow C(S,R) + C(S,R) + CH_2(S) + C(S,R) + C(S,R)$	(100)

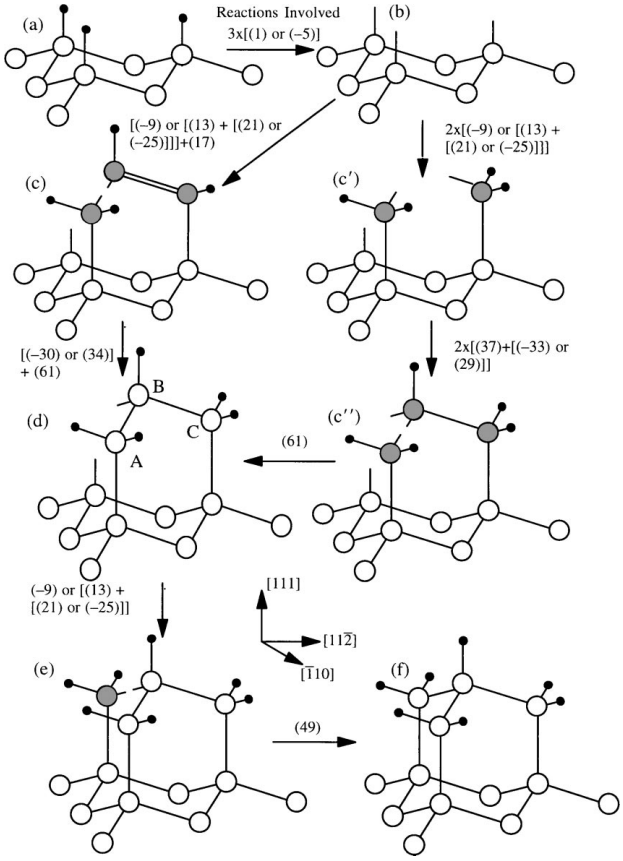

Figure 2 Sequence of steps involved in the nucleation of a new layer on an atomically flat (111) surface. Open circles represent diamond carbon atoms, shaded circles designate hydrocarbon carbon atoms, and small black circles stand for hydrogen atoms. Surface reactions (listed in Table I) involved in various steps of the process are given in parenthesis.

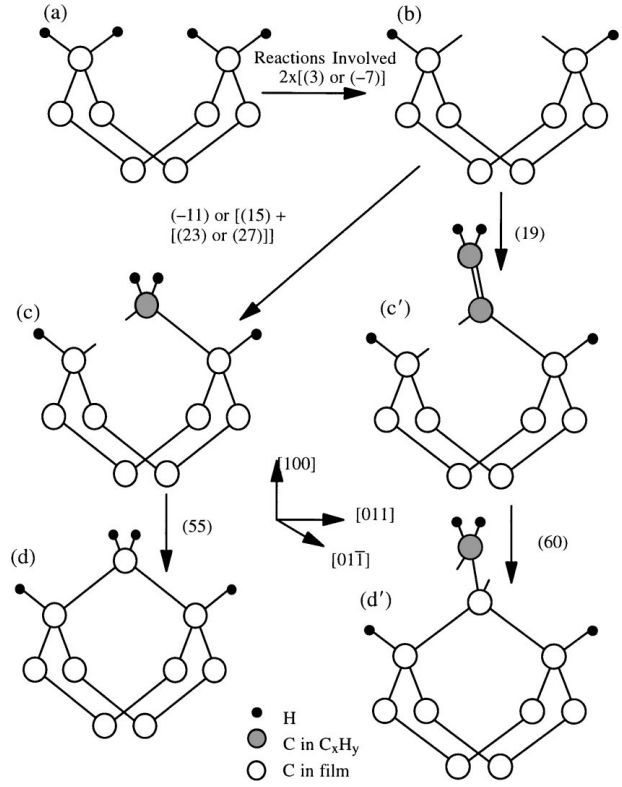

Figure 3 Growth of an (100)-oriented film by trough insertion mechanism. Open circles represent diamond carbon atoms, shaded circles designate hydrocarbon carbon atoms, and small black circles stand for hydrogen atoms. Surface reactions (listed in Table I) involved in various steps of the process are given in parenthesis.

is carried out in order to determine which reactions are critical to (111)-oriented substrates and which to (100)-oriented substrate and which reactions are equally important in both cases. An example of such analysis is shown in Figs 2 and 3. The results of atomic-scale analysis of diamond deposition on (111)- and (100)-oriented films discussed in Section 3 suggest that, to a great extent, the overall deposition rate of (111)-oriented films is controlled by the rate of nucleation of new (111) layers (i.e. the growth rate of the existing layers is relatively high compared to the nucleation rate of new ones). Starting from the assumption that the deposition rate of (111)-oriented films is controlled by the nucleation of new layers, a detailed analysis of the role of various reactions in the nucleation process is carried out. A new layer is nucleated by formation of a three-carbon bridge (e.g. ABC in Fig. 2d). Adsorption of C_2H_2 (contributes two carbon atoms to the bridge) on a surface site adjacent to a site containing an adsorbed hydrocarbon is critical in the nucleation of a new layer. Nucleation of three-carbon bridges through coordinated adsorption of three one-carbon hydrocarbon radicals is much less likely and consequently nucleation paths such as (a)-(b)-(c)-(d)-(e)-(f) in Fig. 2 prevail over the ones such as (a)-(b)-(c′)-(c)″-(d)-(e)-(f) in the same figure. To account for these effects, surface reactions associated with the paths such as: (a)-(b)-(c′)-(c″)-(d)-(e)-(f) are neglected when reactor-scale modeling of CVD of the (111)-oriented films is carried out.

In the case of (100)-oriented films, atomic-scale analysis reveals that nucleation of new layers can begin with adsorption of one-carbon hydrocarbons and thus the nucleation rate is quite high. Since the concentration of such hydrocarbons is generally higher than the concentration of two- or multi- carbon hydrocarbons, reaction paths such as (a)-(b)-(c)-(d) are more significant than the ones such as (a)-(b)-(c′)-(d′), Fig. 3. Consequently, the surface reactions associated with the reaction paths such as (a)-(b)-(c′)-(d′) can be neglected during the reactor-scale analysis of CVD of the (100)-oriented diamond films.

The third column in Table I list the reactions specific to (111)- and (100)-oriented films as well the reactions which are important for both substrate orientations.

2.2. Results

An example of the results which can be obtained by analyzing the CVD of diamond films at the reactor scale is shown in Figs 4 and 5. Fig. 4a and b show the axial and substrate-radius scaled radial velocity fields for CVD of (111)- and (100)-oriented diamond single crystals under the following processing conditions: Reactive gas at the reactor inlet (0.4% CH_4, 92.6% H_2), $T_{\text{heator}} = 2000$ K, $T_{\text{substrate}} = 1000$ K, $p = 20.25$ Torr, Heater-to-Substrate distance $= 1.3$ cm. Fig. 4c and d show the corresponding temperature and gas-phase species concentration fields. The results shown in Fig. 4a–d suggest that the nature of the substrate, i.e. (111)- vs. (100)-oriented substrate, has a measurable

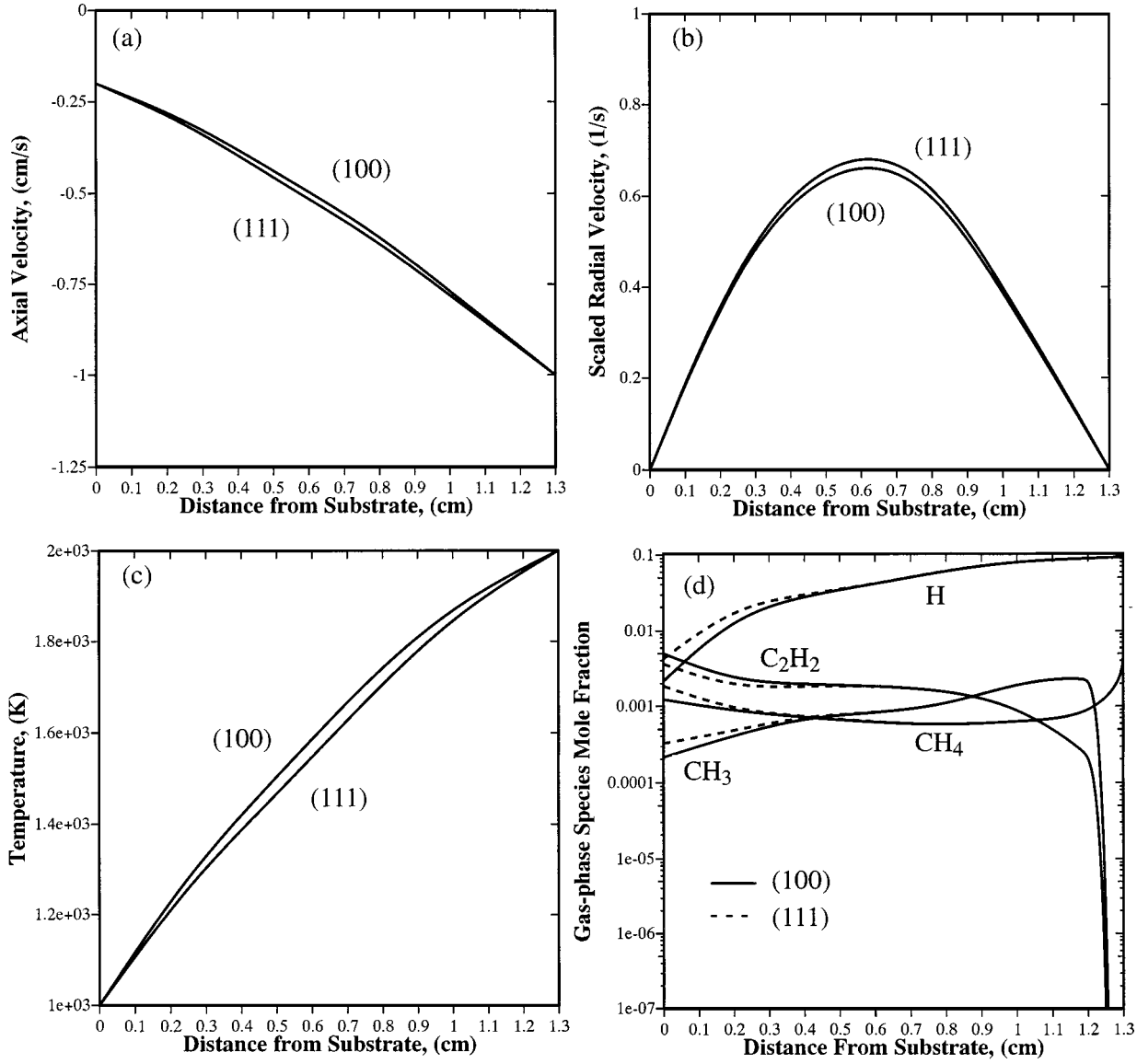

Figure 4 Axial velocity fields, (a), scaled radial velocity fields, (b), temperature fields, (c), and the gas-species concentration fields, (d), as a function of the distance from the (111)- and (100)-oriented diamond substrates under the following CVD condition: Reactive gas at the reactor inlet (0.4% CH_4, 92.6% H_2), $T_{heator} = 2000$ K, $T_{substrate} = 1000$ K, $p = 20.25$ Torr, Heater-to-Substrate distance = 1.3 cm.

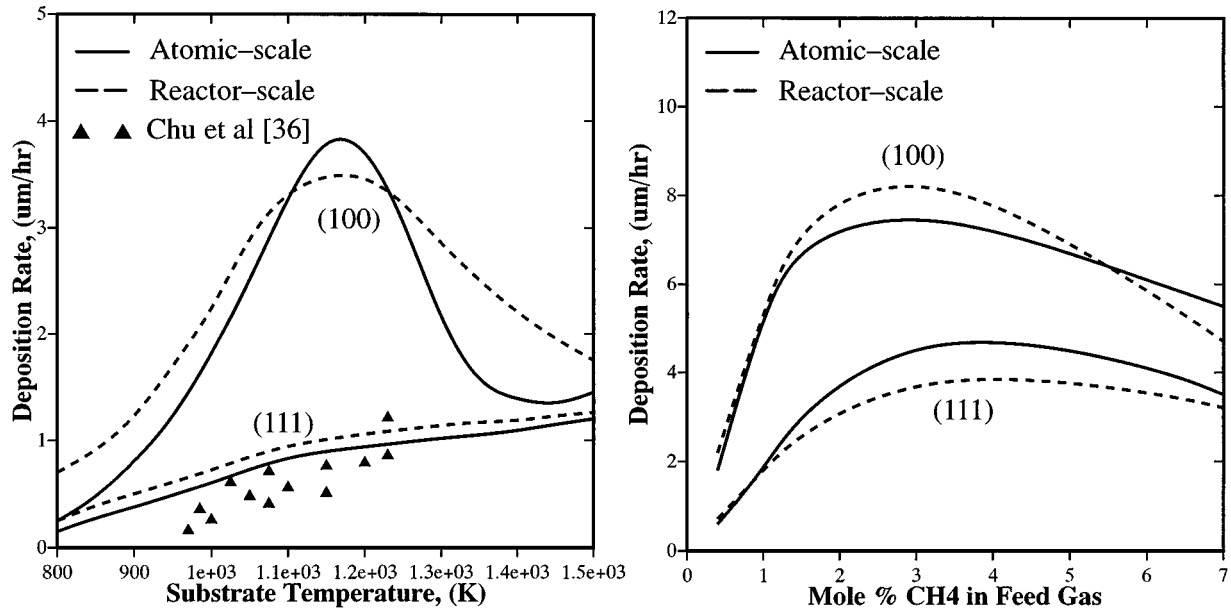

Figure 5 Reactor- and atomic scale analyses predicted (111)- and (100)-oriented film deposition rates as a function of (a) the substrate temperature and (b) concentration of CH_4 in feed gas. The remaining processing condition are as indicated in Fig. 4.

effect on the gas-phase fields. It should be noted, however, that among the results shown in Fig. 4a–d, only the concentration of the gas species at the substrate surface, Fig. 4d, are used as input to the atomic-scale modeling of diamond-film deposition discussed in next section. Fig. 5a and b, respectively, show the effects of substrate temperature and mole fraction of CH_4 in the feed gas on the growth rates of (111)- and (100)-oriented diamond films. The primary purpose of displaying the results in Fig. 5a and b is to enable their comparison with the atomic-scale modeling and experimental counterparts. This comparison is discussed in next section.

3. Atomic-scale modeling of CVD

3.1. General consideration

The growth of (111)- and (100)-oriented single-crystalline diamond films by CVD has been modeled at the atomic scale using rigid diamond-type lattices. In other words, the atomic relaxations and vibrations are not considered. In the case of (111)-oriented films, the orientation of the lattice is defined as: $x = [11\bar{2}]$, $y = [1\bar{1}0]$ and $z = [111]$ while in the case of the (100)-oriented diamond films the lattice orientation is defined as $x = [011]$, $y = [01\bar{1}]$, $z = [100]$. Each film is allowed to grow in the z-direction while periodic boundary conditions are applied in the x and y directions in order to avoid the film-edge effects. The size of the computational lattice in the x-y plane is 90 $d_{(112)} \times 40\ d_{(1\bar{1}0)}$ for the (111)-oriented diamond film and 60 $d_{(011)} \times 40\ d_{(01\bar{1})}$ for the (100)-orientated where $d_{(uvw)}$ is the spacing of the (uvw) diamond planes. Initially, six (111) and six (100) planes of the diamond lattice are filled with carbon atoms to form a six-layer thick (111) and a six-layer thick (100) substrate, respectively. To passivate the top layer of the substrates, the substrates are terminated with a layer of atomic hydrogen (H). A small segment of each of the two substrates is shown in Fig. 6, in which diamond atoms are represented with open circles while hydrogen atoms are denoted as filled circles.

The growth of diamond requires that the hydrogen-terminated substrate surface be activated which can take place either by desorption (Reactions (−5)–(−8), Table I) or by abstraction (e.g. Reactions (1)–(4), Table I) of the chemisorbed atomic hydrogen. Once a substrate surface site is activated, it can be repassivated by chemisorption of either an atomic hydrogen (Reactions (5)–(8), Table I) or a hydrocarbon molecule (e.g. Reactions (13)–(20), Table I). The chemisorbed hydrocarbon molecule can desorb (Reactions (−13)–(−26), Table I) and thus reactivate the site. Conversely, the hydrocarbon molecule may interact with the gas phase (e.g. Reactions (9)–(12), (21)–(40), (−21)–(−24), (−29)–(−32), Table I) or with other surface species (e.g. Reactions (44)–(61), (68), Table I) which ultimately leads to the incorporation of carbon atoms from the hydrocarbon molecule into the diamond lattice and thus to film growth.

Atomic-scale modeling of CVD of diamond is carried out in the present work by quantifying the contribution of the surface reactions listed in Table I to the process of incorporation of carbon from the gas phase into the growing film. To ensure consistency between the atomic- and reactor-scale models, the concentration of gas and surface species on the film surface obtained in Section 2 are used in this section to determine the rates of surface reactions.

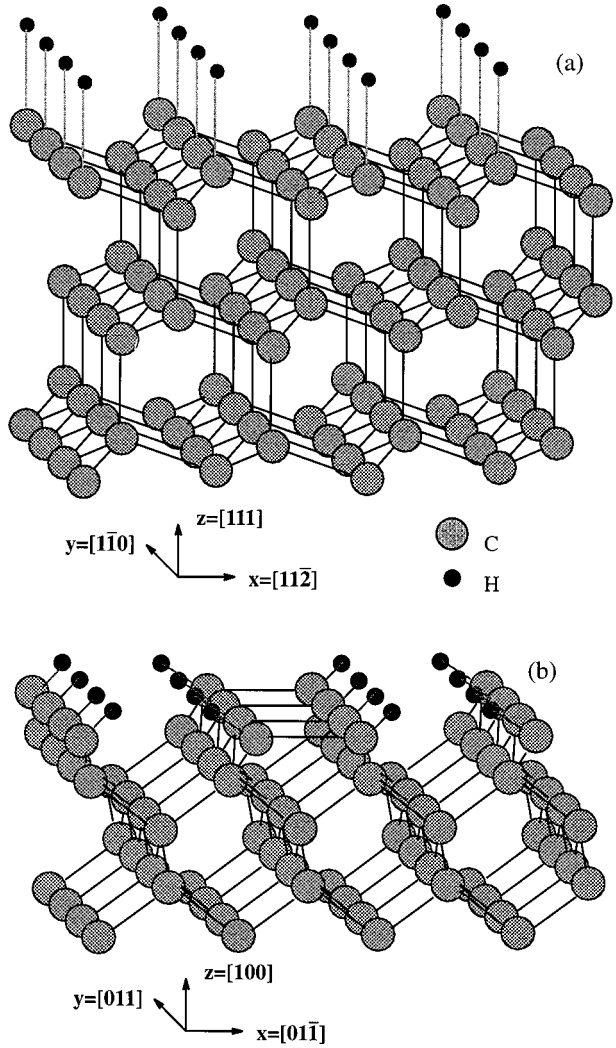

Figure 6 A section of: (a) an (111)-oriented and (b) an (100)-oriented diamond substrate used in the atomic-scale modeling of the diamond CVD process.

The temporal evolution of the diamond film during growth is modeled using the version of the kinetic Monte Carlo method recently developed by Battaile *et al*. [18]. Within this method, one surface reaction is allowed to take place at one surface site during each time step. The occurrence of one of the reactions at one of the sites is termed an event. At each time step, a list of all possible events is constructed and the probability for each event is set proportional to the rate of the associated surface reaction relative to the rates of the surface reactions associated with all the other possible events. In other words, at each time step, a random number α uniformly distributed in the range (0, 1) is generated to select the event m from M possible events in accordance with the relation:

$$\frac{\sum_{j=0}^{m-1} r_j}{\sum_{j=0}^{M} r_J} < \alpha < \frac{\sum_{j=0}^{m} r_j}{\sum_{j=0}^{M} r_j} \qquad (1)$$

where r_j is the rate of surface reaction associated with event j and $r_0 = 0$. r_j corresponds to the either first or the second term on the right hand side of Equation (14), depending on the direction of the particular surface reaction.

After an event has occurred, the total number of possible events M, and the sequence in which the events are listed are updated and the aforementioned procedure is repeated.

The Monte Carlo method used in the present work uses a variable time step to account for the fact that different events take place at different rates. At each simulation step the time increment Δt is computed as:

$$\Delta t = -\frac{\ln(\beta)}{\sum_{i=1}^{M} r_i} \tag{2}$$

where β is a random number uniformly distributed in the range (0, 1), and the denominator in Equation 2 represents the sum of the reaction rates of all the events that can occur in the given simulation step. The time increment given by Equation 2 is adjusted dynamically and stochastically during a Monte Carlo simulation run to accommodate the fastest possible event at each simulation step, thus greatly reducing restrictions associated with conventional fixed time-increment Monte Carlo methods. In other words, when fast reactions are possible in a given step i.e. when the instantaneous deposition rate is high, the denominator in Equation 2 is large and consequently, the time increment Δt is small. Conversely, when the instantaneous deposition rate is low because only slow reactions are possible in a given simulation step, the time increment given by Equation 2 is large.

3.2. Results

The effects of substrate temperature and the mole fraction of CH_4 in the feed gas on the atomic-scale modeling predicted deposition rates of (111)- and (100)-oriented diamond films are shown respectively in Fig. 5a and b for comparison with their reactor-scale modeling counterparts. The atomic-scale modeling deposition rates are obtained by dividing the product of the number of atoms deposited in a given time increment and the (111)/(100) interplanar spacing by the product of the number of carbon atoms in a completely filled (111)/(100)-layer and the time interval. A time increment of 0.01 sec is used to compute the "instantaneous" deposition rate. For comparison, the experimental results of Chu *et al*. [36] for the (111)-oriented films are also included in Fig. 5a. The results depicted in Fig. 5a and b show that the reactor- and atomic-scale modeling results are generally consistent with each other. This is quite encouraging considering: (a) a completely different nature of the two modeling schemes: and (b) that both sets of modeling results are generally in a reasonable good agreement with their experimental counterparts.

The top view of an (111)-oriented diamond film deposited under the same CVD conditions as the ones defined in Section 2.7 at two deposition times is shown in Fig. 7a and b. The surface morphology shown in these figures is typical for the (111)-oriented diamond films. To help the analysis of the surface morphology different shades of grey are used to designate the relative magnitude of the z coordinate of the atoms. The white (the brightest shade of grey) atoms are located on the very top of the surface asperities, while the black (the darkest shade of grey) ones are located on the bottom of the surface valleys. To further improve the clarity of the surface morphology, the twinned regions (T) are represented using circles of somewhat larger diameter. A relatively large fraction of twins separated from the regular regions by dislocations loops (D) and gaps (G) can be observed in Fig. 7a. As is shown in Fig. 2d and further discussed in Part II [20], formation of a new (111) layer starts with the formation of a three-carbon bridge. Such a bridge is marked as B in Fig. 7a. As a bridge grows it forms first a nucleus (N) and then a large islands (I). Large islands, I_1 and I_2 in Fig. 7a and b form well-defined edges (E) and kinks (K). The evolution of the morphology of the islands, I_1 and I_2, with time, Fig. 7a and b, clearly shows that kink nucleation

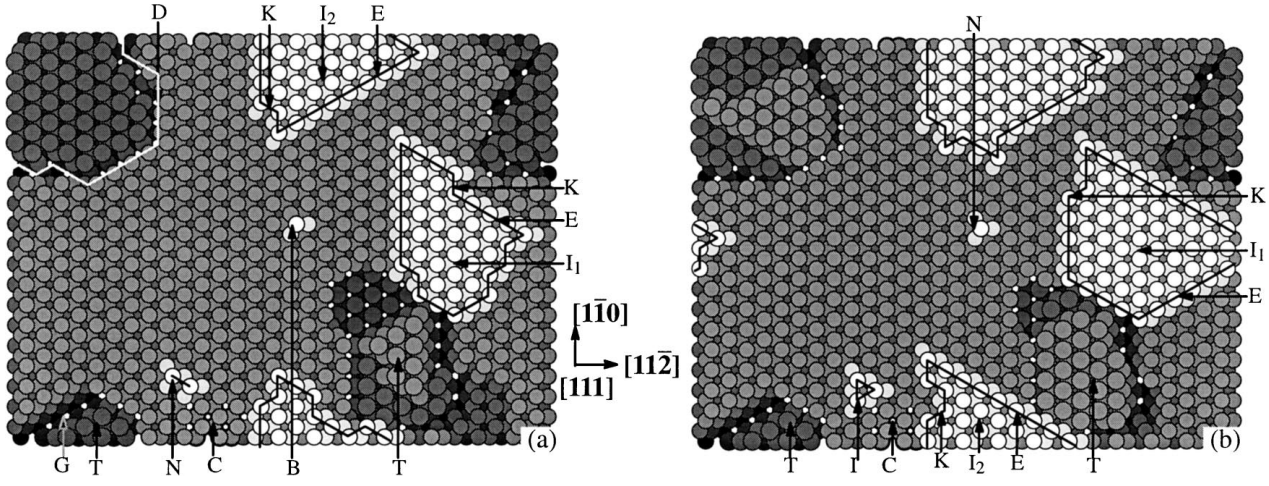

Figure 7 Top view of two (111)-oriented diamond films obtained under the CVD conditions identical to the ones listed in Fig. 4. Deposition times: (a) 1.81 s and (b) 2.07 s. Nomenclature: B – 3-carbon bridge, C – Twin covered by regular crystal, D – Dislocation loop, E – Edge, G – Gap, I – Island, K – Kink, N – Nucleus, T – Twin.

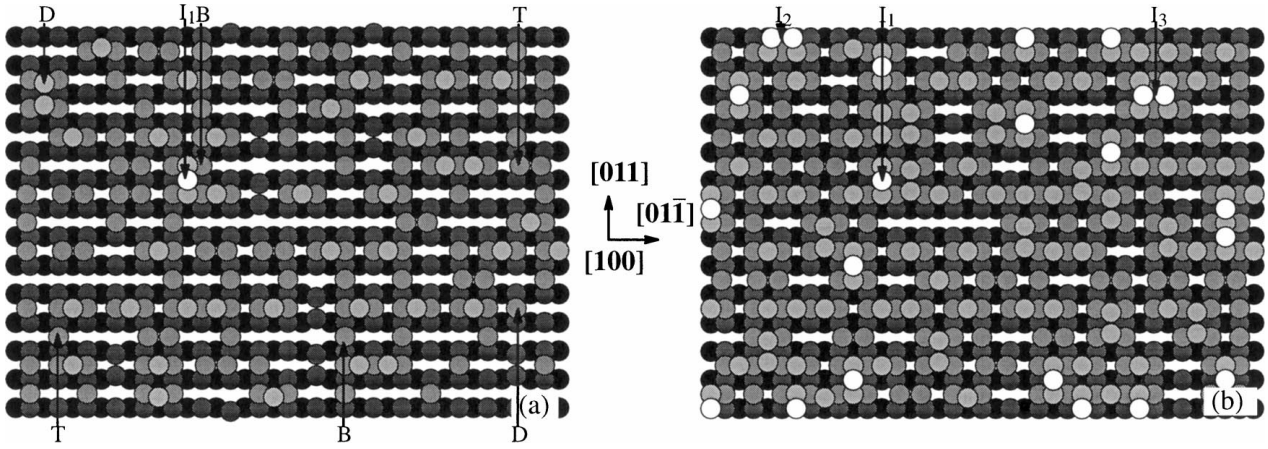

Figure 8 Top view of two (100)-oriented diamond films obtained under the CVD conditions identical to the ones listed in Fig. 4. Deposition times: (a) 0.02 s and (b) 0.03 s. Nomenclature: B—BCN mechanism, D—Dimer insertion mechanism, I—Island, T—Trough insertion mechanism.

and motion are the main mechanisms of island growth. Furthermore, the rate of growth of the existing islands is found to be substantially larger than the rate of nucleation of the new (111) layers. This has two major consequences: (a) the overall deposition rate is governed by the rate of nucleation of new (111) layers and (b) the surface morphology is dominated by (111)-islands, edges and kinks.

It should be noted that since the regular (non-twinned) regions constitute the largest portion of the film surface and since the growth is nucleation controlled, the regular regions grow at a higher rate than the twinned regions. As a result, the twinned regions are gradually being covered with the regular regions (C), and become buried inside the film.

The top view of an (100)-oriented diamond film deposited under the identical conditions as the (111)-oriented diamond film discussed above is shown in Fig. 8a–b. In order to indicate the formation of dimer bonds along the [011] direction, the distance between the carbon atoms forming a dimer bond is shortened. A striking feature of the surface morphologies shown in Fig. 8a and b is the absence of well-defined regularly-shaped islands surrounded by straight edges and kinks, which were seen in Fig. 7a and b. Instead, typical islands, I_1, I_2, I_3 in Fig. 8a and b, are quite irregular in shape and the film grows by the continuing nucleation of new and the growth of the existing islands. Consequently, the film surface remains very irregular. A careful analysis of the deposited surface in Fig. 8a reveals that all three deposition mechanism: the dimer insertion (D), the trough insertion (T) and the BCN mechanism (B) are operative and their relative contribution to the film deposition process is assessed as: $D:T:B \cong 16:7:6$.

4. Discussion and conclusions

In the present work, chemical vapor deposition of the (111)- and (100)-oriented single-crystalline diamond films is analyzed by combining a continuum reactor-scale model with a discrete atomic-scale model. It is shown that by proper coupling the two models can make consistent predictions for the film growth rate over wide ranges of processing conditions. Based on this finding and the fact that processing parameters are used as input in the reactor-scale model and the film microstructure is the output of the atomic-scale model, the present approach enables the establishment of the processing/microsctructure (and, in turn, property) relationship in single crystalline diamond films. In other words, the approach allows processing condition to be selected to obtain the film of desired microstructure and properties.

The atomic-scale modeling results presented in the present paper reveal a distinct differences in the surface morphology and surface-reaction kinetics of (111)- and (100)-oriented diamond single crystals. The surface morphology of (111)-oriented films is dominated by islands of the new layer bounded by straight-edges and kinks while in the case of (100)-oriented films the surface is composed mostly of small clusters of the new layer and is hence quite irregular. The overall deposition rate in the case of (111)-oriented films is governed by the nucleation of new (111)-layers while in the case of (100)-oriented films both the nucleation and growth surface processes appear equally important. As will be shown in Part II [20], these differences are intimately linked with differences in the nature and concentration of the defects produced in the course of the deposition process.

Appendex: Modeling of CVD in a rotating-disk reactor

Physical model

The CVD reactor is modeled as a rotating disk of infinite extent in the r-θ plane located at the axial position $z = 0$, Fig. 1, and separated in the axial direction from a parallel porous stationary heater by a distance L. A forced, purely axial flow from the heater is directed toward the disk. The flow at the heater is approximated by the inlet flow conditions into the reactor. Due to the finite domain dimension in the z direction, a radial pressure gradient is developed. The non-isothermal reacting-flow boundary value problem is defined by a set of governing conservation equations. In these equations, both convective and diffusive transport of species are considered as well as the production/consumption of species by the chemical reactions. Thermal diffusion is taken into account in thermal energy conservation

and species continuity equations. Transport properties are considered as temperature and mixture-composition dependent.

Nomenclature

A_i, β_i, E_i	Arrhenius coefficients in the forward rate constant of the i-th reaction
A_{in}	Cross-section area of the reactor inlet
c_{p}, c_{pk}	Specific heat at constant pressure for the gas mixture and k-th species, respectively
h_k	Specific enthalpy of the k-th species
I_{g}, I_{s}	Total number of gas-phase and surface reactions, respectively
$k_{\text{f}i}$, $k_{\text{r}i}$	Forward and reverse rate constants for the i-th reaction, respectively
K_{b}, K_{g}, K_{s}	Total number of bulk, gas and surface species, respectively
$\dot{m}$	Mass flow rate at the reactor inlet
$\bar{M}$	Mean molecular weight of a mixture
M_k	Molecular weight of the k-th species
R_{c}	Universal gas constant
$\dot{s}_k$	Production rate of the k-th species due to surface reactions
t	Time
T	Temperature
T_{in}	Temperature at the reactor inlet
u, v, w	Axial, radial and circumferential velocities, respectively
V_k	diffusion velocity of the k-th species
Y_k	Mass fraction of the k-th species
λ	Thermal Conductivity
ϱ	Mass density
$\dot{\omega}_k$	Chemical production rate of the k-th species due to gas-phase reactions

Boundary value problem and governing equations

The boundary value problem is defined in terms of z as the independent variable and $u(z)$, $V(z) \equiv v(z)/r$, $W(z) \equiv w(z)/r$, $T(z)$, $Y_k(z)$, $k = 1, \ldots, K_{\text{g}} - 1$, as dependent variables and the following governing equations:

Mixture continuity/mass conservation:

$$\frac{1}{\varrho}\frac{\partial \varrho}{\partial t} = -\frac{\partial u}{\partial z} - 2V - \frac{u}{\varrho}\frac{\partial \varrho}{\partial z} = 0 \qquad \text{(A1)}$$

Radial momentum conservation:

$$\varrho\frac{\partial V}{\partial t} = \frac{\partial}{\partial z}\left(\mu\frac{\partial V}{\partial z}\right) - \varrho u\frac{\partial V}{\partial z} - \varrho(V^2 - W^2) - \frac{1}{r}\frac{\mathrm{d}p_{\text{m}}}{\mathrm{d}r} = 0 \qquad \text{(A2)}$$

Circumferential momentum conservation:

$$\varrho\frac{\partial W}{\partial t} = \frac{\partial}{\partial z}\left(\mu\frac{\partial W}{\partial z}\right) - \varrho u\frac{\partial W}{\partial z} - 2\varrho V W = 0 \qquad \text{(A3)}$$

Thermal energy balance:

$$\varrho c_{\text{p}}\frac{\partial T}{\partial t} = \frac{\partial}{\partial z}\left(\lambda\frac{\partial T}{\partial z}\right) - \varrho c_{\text{p}} u\frac{\partial T}{\partial z} - \sum_{k=1}^{K_{\text{g}}}\left(c_{pk}\varrho Y_k V_k\frac{\partial T}{\partial z} + \dot{\omega}_k h_k\right) = 0 \qquad \text{(A4)}$$

Species continuity:

$$\varrho\frac{\partial Y_k}{\partial t} = -\frac{\partial \varrho Y_k V_k}{\partial z} - \varrho u\frac{\partial Y_k}{\partial z} + M_k\dot{\omega}_k = 0 \quad (k = 1, \ldots, K_{\text{g}} - 1) \qquad \text{(A5)}$$

The following simplifications are used: (a) constant angular velocity at $z = \text{const}$; (b) stagnation flow approximation for the circumferential velocity: $v(z, r) = V(z)r$; (c) constant average thermodynamic pressure, p; (d) non-zero constant radial gradient of spatially varying pressure, $\mathrm{d}p_{\text{m}}/\mathrm{d}r = \text{const}$ and the ideal-gas equation of state is applicable:

$$\varrho = \frac{p\bar{M}}{RT} = \frac{p}{R_{\text{c}}T}\sum_{k}^{K_{\text{s}}}\frac{Y_k}{M_k}.$$

Since $\varrho = \varrho(T, Y_k, k = 1, \ldots, K_{\text{g}})$, ϱ is not considered as a separate dependent variable.

Chemical production rate of the k-th gas-phase species is defined as:

$$\dot{\omega}_k = \sum_{i=1}^{I_{\text{g}}}\nu_{ki}q_i = \dot{\omega}_k(Y_j(j = 1, \ldots, K_{\text{g}})) \quad (k = 1, 2, \ldots, K_{\text{g}}) \qquad \text{(A6)}$$

where ν_{ki} is the net stoichiometric coefficient for the k-th species in the i-th reaction:

The rate of progress for the i-th gas-phase chemical reaction is defined as:

$$q_i = k_{ki}\prod_{k=1}^{K_{\text{g}}}[X_k]^{\nu'_{ki}} - k_{\text{r}i}\prod_{k=1}^{K}[X_k]^{\nu''_{ki}} \quad (i = 1, \ldots, I_{\text{g}}) \qquad \text{(A7)}$$

where $[X_k]$ is molar concentration for k-th gas-phase species, $k_{\text{f}i}$ and $k_{\text{r}i}$ the forward and the reverse rate constants for the i-th chemical reaction expressed as:

$$k_{\text{f}i} = A_i T^{\beta_i}\exp\left(\frac{-E_i}{R_{\text{c}}T}\right) \qquad \text{(A8)}$$

$$k_{\text{r}i} = \frac{k_{\text{f}i}}{K_{\text{c}i}} \qquad \text{(A9)}$$

and the equilibrium constant for the i-th chemical reaction in concentration units $K_{\text{c}i}$ is defined in terms of the corresponding entropy and enthalpy changes [19].

The following boundary conditions are applied to the problem at hand:

At the Heater: (a) axial velocity at the inlet is defined in terms of the equation of state as:

$$u = -\frac{\dot{m}RT_{\text{in}}}{MpA_{\text{in}}} = -\frac{\dot{m}RT_{\text{in}}}{pA_{\text{in}}}\sum_{k=1}^{K_{\text{g}}}\frac{Y_k}{M_k};$$

(b) no radial flow; (c) no circumferential flow; (d) constant temperature and (e) constant inlet-gas species mass fractions.

At the Substrate: (a) the axial velocity is defined through the Stefan flow condition;

$$u = \frac{1}{\varrho}\sum_{k=1}^{K_{\text{g}}}\dot{s}_k^{\text{gas\_on\_surf}}M_k \qquad \text{(A10)}$$

(b) no slip; (c) constant substrate temperature; (d) mass fractions of the gas-phase species are defined in terms of the gas-phase species mass flux balance condition:

$$\varrho Y_k^{\text{sub}}(V_k + u) = \dot{s}_k^{\text{gas\_on\_surf}}M_k \qquad (k = 1, \ldots, K_{\text{g}} - 1) \quad \text{(A11)}$$

Computational strategy

The computational domain between the heater and the substrate is divided into n intervals which yields $n + 1$ discrete z values (nodes), $n - 1$ of which are "internal" nodes.

There are $4 + (K_{\text{g}} - 1) = 3 + K_{\text{g}}$ governing differential equations: (a) one mixture continuity equation, Equation A1; (b) two momentum conservation equations, Equations A2 and A3; (c) one thermal energy conservation equations, Equation A4 and (d) $K_{\text{g}} - 1$ species continuity equations, Equation A5. If each of these equations is written using the appropriate finite difference expressions at $n - 1$ internal nodes, one obtains $(3 + K_{\text{g}})(n - 1)$ algebraic equations.

There are $3 + K_{\text{g}}$ "continuum" unknowns: u, V, W, T, Y_k (k=1, ..., $K_{\text{g}} - 1$). If these variables are given at the heater and at the substrate as the boundary conditions then the total number of discrete unknowns (at $n - 1$ internal nodes) is $(3 + K_{\text{g}})(n - 1)$. Thus the number of unknowns and the number of equations are the same as required.

In the present case, the boundary conditions are defined as following. At the heater u, V, W, T, Y_k ($k = 1, \ldots, K_{\text{g}} - 1$) are all given explicitly. At the substrate, on the other hand, only V, W and T are given explicitly. u and Y_k ($k = 1, \ldots, K_{\text{g}} - 1$) are given only implicitly, through the Stefan flow and the species mass flux balance, respectively. Thus, K_{g} boundary conditions at the substrate needs to be defined. However the equations used to define these conditions introduce additional $K_{\text{s}} - 1$ unknown surface-species site fractions Z_k and $K_{\text{b}} - 1$ unknown bulk-species activities a_k. Therefore the total number of unknown conditions at the substrate is $K_{\text{g}} + (K_{\text{s}} - 1) + (K_{\text{b}} - 1) = K_{\text{g}} + K_{\text{s}} + K_{\text{b}} - 2$. The necessary $(K_{\text{g}} + K_{\text{s}} + K_{\text{b}} - 2)$ equations can be defined from the conditions that at steady state the production rates of the surface species are zero and the the activity of bulk species remains constant and include Equations A10 and A11. The problem can then be solved in a straightforward manner to yield the distribution of u, V, W, T and Y_k ($k = 1, \ldots, K_{\text{g}} - 1$) in the gas-phase between the heater and the substrate, and the concentration of the gas species Y_k ($k = 1, \ldots, K_{\text{g}} - 1$), surface species Z_k ($k = 1, \ldots, K_{\text{s}} - 1$) and bulk species a_k ($k = 1, \ldots, K_{\text{b}} - 1$) on the substrate. The deposition rate of each of the bulk species can next be obtained from its production rate at the surface as:

$$G_k = \frac{\dot{s}_k^{\text{bulk}}M_k}{\varrho_k} \quad (k = 1, K_{\text{b}}) \qquad \text{(A12)}$$

Acknowledgements

The work presented here has been supported by the U.S. Army Research Office, Grant DAAH04-96-1-0197 and Grant DAAD19-99-1-0096. The authors are indebted to Dr. David M. Stepp of ARO for the continuing interest in the present work. Encouragement and friendship of Prof. R. J. Diefendorf is greatly appreciated. The authors also acknowledge the support of the Office of High Performance Computing Facilities at Clemson University.

References

1. K. E. SPEAR, *J. Amer. Ceram. Soc.* **72** (1989) 171.
2. J. E. BUTLER and R. L. WOODIN, *Philos. Trans. R. Soc. London, Ser. A* **342** (1993) 209.
3. D. G. GOODWIN and J. E. BUTLER, in "Handbook of Industrial Diamonds and Diamond Films," edited by M. A. Prelas, G. Popovici and L. K. Bigelow (Dekker, New York, 1997) p. 527.
4. M. E. COLTRIN, R. J. KEE and G. H. EVANS, *J. Electrochem. Soc.* **136** (1989) 819.
5. M. E. COLTRIN, R. J. KEE and F. M. RUPLEY, *International J. of Chemical Kinetics* **23** (1991) 111.
6. D. W. BRENNER, *Phys. Rev. B* **42** (1990) 9458.
7. B. J. GARRISON, E. J. DAWNKASKI, D. SRIVASTAVA and D. W. BRENNER, *Science* **255** (1992) 835.
8. D. HUANG and M. FRENKLACH, *J. Phys. Chem.* **96** (1992) 1868.
9. V. I. GAVRILENKO, *Phys. Rev. B* **47** (1993) 9556.
10. Y. L. YANG and M. P. D'EVENLYN, *J. Amer. Chem. Soc.* **114** (1992) 2796.
11. T. FRAUENHWIM, U. STEPHAN, P. BLAUDECK, D. POREZAG, H.-G. BUSMANN, W. ZIMMERMANN-EDLING and S. LAUER, *Phys. Rev. B* **48** (1993) 18189.
12. Z. JING and J. L. WHITTEN, *Surf. Sci.* **314** (1994) 300.
13. S. SKOKOV, C. S. CARMER, B. WEINER and M. FRENKLACH, *Phys. Rev. B* **49** (1994) 5662.
14. S. CIRACI and I. P. BATRA, *ibid.* **15** (1977) 3254.
15. S. F. YANG, D. A. DRABOLD and J. B. ADAMS, *ibid.* **48** (1993) 5261.
16. B. N. DAVIDSON and W. E. PICKETT, *ibid.* **49** (1994) 11253.
17. M. M. CLARK, L. M. RAFF and H. L. SCOTT, *Comput. Phys.* **10** (1996) 584.
18. C. C. BATTAILE, D. J. SROLOVITZ and J. E. BUTLER, *J. Appl. Phys.* **82**(12), (1997).
19. M. GRUJICIC and S. G. LAI, *Journal of Material Science* **34**(i1) (1999) 7.
20. *Idem., Journal of Material Science*, submitted.
21. G. EVANS and R. GREIF, *J. Heat Trans. ASME* **109** (1987) 928.
22. T. VON KARMAN and A. ANGEW, *Math. Mech.* **1** (1921) 233. Also available as NACA-TM-1092.

23. F. M. WHITE, "Viscous Fluid Flow" (McGraw-Hill, New York, 1974).
24. H. SCHHLICHTING, "Boundary Layer Theory," 7th ed. (McGraw-Hill, New York, 1979).
25. W. G. COCHRAN, *Proc. Cambridge Phil. Soc*. **30** (1934) 365.
26. E. M. SPARROW and J. L. GREGG, *J. Heat Trans. ASME* **82** (1960) 294.
27. D. R. OLANDER, *I. and E. C. Fund*. **6** (1967) 178.
28. *Idem., ibid*. **6** (1967) 188.
29. R. POLLARD and J. NEWMAN, *J. Electrochem. Soc.* **127** (1980) 744.
30. M. L. HITCHMAN, B. J. CURTIS, H. R. BRUNNER and V. EICHENBERGER, "Physicochemical Hydradynamics, Vol. 2," edited by D. B. Spalding (Advanced Publications, London, 1977).
31. G. EVANS and R. GREIF, *Num. Heat Transfer* **12** (1987) 243.
32. M. E. COLTRIN and D. S. DANDY, *J. Appl. Phys*. **74**(9) (1993) 5803.
33. R. J. KEE, F. M. RUPLEY and J. A. MILLER, Sandia National Laboratories Report SAND89-8009 (1989).
34. C. WILD, P. KOIDL, W. MÜLLER-SEBERT, H. WALCHER, R. KOHL, N. HERRES and R. LOCHER, *Diamond and Related Materials* **2** (1993) 158.
35. C. C. BATTAILE, D. J. SROLOVITZ and J. E. BUTLER, *J. of Elec. Mater*. **26**(9) 1997.
36. C. J. CHU, R. H. HAUGE, J. L. MARGRAVE and M. P. D'EVELYN, *Appl. Phys. Lett*. **61** (1992) 1393.

Received 12 August 1999
and accepted 30 March 2000